 CMES, vol.85, no.3, pp.239-277, 2012

Rigorous Joining of Asymptotic Beam Models to Three-Dimensional Finite Element Models

Huimin Song[1], **and Dewey H. Hodges**[1]

Abstract: The present paper presents a rigorous approach that can accurately and efficiently capture the linear, static and free-vibration behaviors of a beam-like structure by the rigorous combination of a one-dimensional beam model with a three-dimensional continuum model. This study focuses on coupling these disparate finite element types, putting them both into a single finite element model while making use of the asymptotically exact information available as part of the beam model, which itself is obtained by asymptotic dimensional reduction. The coupling is undertaken by use of appropriate transformation matrices at the interface together with stress and displacement recovery relations that are part of the beam theory. Results obtained from the so-called joined model" are compared with those from a finely meshed model using three-dimensional brick elements. It is demonstrated that the present approach provides accurate solutions for effects previously available only from three-dimensional models. However, because the joined model uses far fewer elements than a full three-dimensional model, the joined model is more efficient.

Keywords: Finite Element, Joining 3D-1D, Asymptotic Beam, Transformation matrix.

1 Introduction

In the aerospace and automotive industries, many finite element analysis use lower-dimensional finite elements, such as beams, plates and shells. These simplified models can greatly reduce computational effort; however, reduced-dimensional models may introduce inaccuracies, particularly at points near boundaries, discontinuous properties and near portions of the structure where such models may not apply. The present study proposes the use of models based on a beam theory that is derived asymptotically and coupled with three-dimensional (3D) finite element

[1] Daniel Guggenheim School of Aerospace Engineering, Georgia Institute of Technology, Atlanta, Georgia 30332-0150

models. In particular, the beam theory should be used over all parts of a complex structure that allow it, while 3D finite elements should be reserved for all other parts of the structure. The reduced-order model and the 3D model are assembled together to obtain the solution. In this way, a complex structure can be analyzed making maximum use of simple models without the loss of accuracy presently incurred in dimensionally-reduced models near boundaries and discontinuities or when they are joined to inherently 3D structures.

There exist several methods that focus on combining finite element models of mixed dimensionality. These methods can be divided into two main categories. One is based on using transition elements at the interface between the different types of elements, and the other on using multi-point constraints at the interface.

1.1 Constructing transition elements

[Surana (1979)] presented the first isoparametric transition elements, which were developed for cross-sectional properties and stress analysis of beams with cross sections that consist of both thin-walled and solid sections. In his subsequent papers [Surana (1980a,b, 1982)], isoparametric transition elements were developed for linear elastic axisymmetric, 3D stress analysis and further extended for geometrically nonlinear analysis, respectively. [Cofer and Will (1991)] proposed a transition element that can connect quadratic, isoparametric solid finite elements to shell finite elements. [Gmür and Schorderet (1993)] proposed a set of transition elements connecting 3D standard isoparametric solid finite elements and superparametric shell finite elements for structural dynamics. [Chavan and Wriggers (2004)] developed a finite element formulation of a transition element for consistent coupling between shell and beam finite element models of thin-walled beam-like structures in thermoelastic problems.

Most of the above methods only deal with the coupling between solid elements and shell elements. Although solid-to-shell transition elements have been available for more than twenty years, only a few works have proposed solid-to-beam transition elements. For instance, on the basis of [Gmür and Schorderet (1993)], [Gmür and Kauten (1993)] presented 3D solid-to-beam transition elements for structural dynamics analysis. Later [Dohrmann and Key (1999)] proposed a transition element for uniform strain hexahedral and tetrahedral finite elements. [Dohrmann, Key, and Heinstein (2000)] developed methods for connecting dissimilar 3D finite element meshes. Two years later, [Garusi and Tralli (2002)] developed a transition elements for modeling solid-to-beam and plate-to-beam connections based upon the hybrid stress method.

From the 3D solid-beam analyses described above one can obtain good agreement on stress or frequency results between such mixed models and 3D finite element

models. However, only beams with simple cross sections such as rectangular and circular cross sections have been analyzed. Although [Garusi and Tralli (2002)] analyzed a thin-walled beam with a C-shape cross section, they assumed a Saint-Venant warping function from the theory of elasticity. For beams with complex cross sections such as helicopter and wind turbine rotor blades, the cross-sectional properties and warping functions cannot be obtained by using the above methods.

1.2 Multi-Point Constraints

Compared to transition elements, coupling methodology based on the so-called multi-point constraint (MPC) is simpler to implement. The early developments include works of [Curiskis and Valliappan (1978); Abel and Shephard (1979)]. [Curiskis and Valliappan (1978)] presented a general solution algorithm for the incorporation of a general set of linear constraint equations into a linear algebraic system. [Abel and Shephard (1979)] developed a method of introducing general constraint equations into finite element matrix equations. The methods are suitable for application in minicomputer implementations of finite element analysis unless a large number of constraints is to be applied. Later [Shephard (1984)] presented a procedure for the application of linear multi-point constraints. The procedure employs the transformation approach for constraint application, which reduces the number of equations to be solved by the number of constraints.

Due to the appearance of large computers, MPCs are more and more widely used in finite element analysis. NASA Langley Research Center has developed a method for analyzing structures composed of two or more independently modeled substructures, based on a hybrid variational formulation with Lagrange multipliers, and applied it to global/local demonstration problems for one-dimensional (1D), [Aminpour, Ransom, and McCleary (1992); Ransom, McCleary, and Aminpour (1993); Aminpour, Ransom, and McCleary (1995); Housner, Aminpour, DVavila, Schiermeier, Stroud, Ransom, and Gillian (1995)] and two-dimensional (2D) [Aminpour and Krishnamurthy (1997)] interfaces. NASA has also developed the technology for a solid-to-shell transition element for use with composites [Davila (1994)], and has combined it with the 1D interface element. Based on earlier work, [Schiermeier, Kansakar, Mong, Ransom, Aminpour, and Stroud (2002)] demonstrated several simple models illustrating global/local analysis using p-version interface elements in MSC.Nastran. Among those examples only the shell-to-solid coupling results are available in [Schiermeier, Kansakar, Mong, Ransom, Aminpour, and Stroud (2002)].

Compared to the use of MPCs on shell-to-solid interfaces, coupling of beam elements by MPC is undertaken in only a few papers. For instance, [Avdeev, Borovkov, Kiylo, Lovell, and Jr (2002)] presented a finite element approach to model edge ef-

fects in beam sandwich structures. The approach is based on coupled 2D and 1D formulations in which the joining is accomplished by means of a penalty function method. The accuracy of the proposed method, however, strongly depends upon the correct determination of the penalty factor. A formulation coupling 3D solid and 1D beam formulations is not available in [Avdeev, Borovkov, Kiylo, Lovell, and Jr (2002)]. [Monaghan, Doherty, Court, and Armstrong (1998)] developed a scheme for establishing compatibility and equilibrium at the interface between 1D beam and 3D solid finite element models. Multi-point constraint equations were obtained by equating the work done by the stresses in each part of the model at the interface between the models. These equations were implemented using standard multi-point constraint capability, such as the EQUATION command in the ABAQUS commercial package. In the reduced-dimensional part an assumed linear variation of the stresses over the plate thickness or beam section is used. [McCune, Armstrong, and Robinson (2000)] extended the method used in [Monaghan, Doherty, Court, and Armstrong (1998)] to the coupling of beams and shells and the coupling of 3D solids and 2D plates. [Shim, Monaghan, and Armstrong (2002)] presented several examples using the same method as in [Monaghan, Doherty, Court, and Armstrong (1998); McCune, Armstrong, and Robinson (2000)].

The 3D solid-beam analysis shown in [Shim, Monaghan, and Armstrong (2002)] used classical beam theory to predict a bending stress distribution on the beam cross section. The shear stress distribution comes from the St. Venant torsion analysis of the beam cross section, but warping is not considered. Based on the theory developed in [Monaghan, Doherty, Court, and Armstrong (1998); McCune, Armstrong, and Robinson (2000); Shim, Monaghan, and Armstrong (2002)], [T.T. Robinson and R.Fairey (2011)] present an automatic procedure to create mixed dimensional finite element models. The technique is applicable to thin walled components with local complex features and automatically creates analysis models where 3D elements representing the complex regions in the component are embedded in an efficient shell mesh representing the mid-faces of the thin sheet regions.

1.3 Other methods

[N. Osawa and Suzuki (2007)] demonstrated a simple, robust and high-precision method for shell-solid coupling on the analysis for fatigue assessment of ship structure. The coupling is implemented by fictitious perpendicular shell planes.

In the practical analysis, shell-solid coupling by rigid link such as RBE2 function of MSC. Nastran is frequently employed as an alternative to the precise MPC coupling, as point out in [N. Osawa and Suzuki (2007)], the superfluous constraint in the direction of the plate thickness applied by the rigid link sometimes causes a large stress perturbation near the interface. There is considerable uncertainty as to

the accuracy of local stress evaluated by rigid link technique.

There is another "rigid link" method, which connect 3D elements with beam elements as shown in [Chung and Sotelino (2006)]. Different from the above two categories and the proposed method which connect the disparate elements at the beam cross-section, the rigid link method connect the beam longitudinal upper or bottom surface to the 3D models.

[Sylvain Bournival (2010)] presented a mesh-based solution to couple beams and solids only using specific arrangements of classical 1D and 3D finite elements without requiring the use of additional constraint equations, therefore neither of the warping or the shear effects are considered in their method.

1.4 Recent applications of mixed dimensional methods

The developed mixed dimensional methods have been widely applied in many engineering analysis. [P. Mata and Oller (2008)] developed a two-scale approach for obtaining the nonlinear dynamic response of RC buildings with local non-prismatic parts. Reduced dimensional elements are used globally and full 3D models are used for local parts with local parts with complex geometry. The dimensional-coupling between scales is performed imposing the kinematics hypothesis of the beam model on surface-interfaces of the 3D model.

[Leon S. Johansen and Kleist (2009)] proposed a two-step approach to obtain the maximized safety against failure in geometrically non-linear laminated composite structures. The three dimensional finite element model was first discretized using single layer shell elements and then refined through the thickness in localized zones, and displacement continuity is enforced through constrain equations.

[E.Wyart and F.Lani (2009)] used a substructured finite element method to compute the stress intensity factors in thin walled structures containing cracks. The structure is decomposed into a domain modeled with classical shell elements and a cracked domain modeled using three-dimensional extended finite elements.

[Kavous Jorabchi and Suresh (2009)] developed an implicit dimensional reduction method in virtual product design. This implicit dimensional reduction is achieved through an algebraic process using a coarse discretization of the domain.

[Ahn and Basu (2011)] proposed a mixed-model approach to analyze cracked metal plates with patch repair. In the mixed-model, a p-convergent transition element is developed to connect the p-convergent high-precision elements for three-dimensional response and p-convergent equivalent single layer elements for two-dimensional response.

1.5 The proposed method

In this paper, we present an approach for joining 3D and beam models at an interface cross section for both static and dynamic analysis of beam-like structures, hereafter referred to as the joined 3D-beam approach. The joined 3D-beam approach:

1. divides the whole structure into 3D parts and beam parts according to boundaries and geometries of the various parts
2. uses an asymptotically exact beam theory, including elastic constants and recovery relations
3. obtains the transformation matrix from asymptotically exact stress recovery equations
4. gets the stiffness matrices and mass matrices for each part
5. assembles them by using transformation matrices at the interfaces
6. solves the assembled system

The derivation of the governing equations is based on a beam model, with the portion near the root end joined to a 3D model and the remainder modeled as a beam. This derivation is then extended to obtain the governing equations for structures that have more than one 3D part and more than one beam part. The beam cross-sectional properties, warping functions and recovery relations are available from VABS (Variational Asymptotic Beam Sectional Analysis), a finite-element-based computer program that implements beam theories [Yu, Hodges, Volovoi, and Cesnik (2002); Yu, Volovoi, Hodges, and Hong (2002); Yu and Hodges (2004, 2005); Hodges (2006)] based on the variational-asymptotic method [Berdichevskii (1979)].

The governing equations for the whole system are obtained by connecting the 3D models and the beam models with transformation matrices at the interfaces. The governing equations of the whole structure are solved as one system. Although the current examples are linear isotropic models, the method can be extended to nonlinear, composite beam-like models. The present approach should give accurate results for finding the effects of 3D constraints at beam boundaries, problems in which beam models give inaccurate results. Finally, the asymptotically correct warping functions at the interface are used to construct the transformation matrix, which should make the current method more accurate than existing methods. It was decided to not make use of Lagrange multipliers because we hoped to not have to eliminate them. The chosen method allowed us to circumvent that step. However, planned future work includes extending the method to include geometric nonlinearity, which will allow for straightforward evaluation of the two approaches.

In this paper the theoretical foundation of the methodology is outlined first. Then, the development of the transformation matrix is presented. After providing the formulation of the Timoshenko beam, we provide four joined 3D-beam examples that treat the static response, free-vibration frequencies, effects of different boundary constraints, and a beam model with geometric nonuniformity, respectively.

2 General Methodology and Approach

2.1 Static formulation

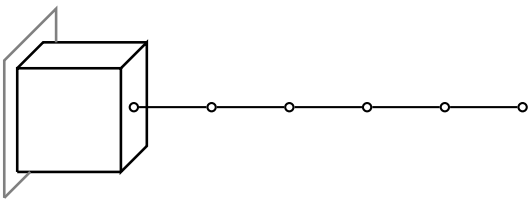

Figure 1: Joined 3D-beam example with one 3D part and one beam part

First, consider a joined model with only one 3D part and one beam part as shown in Fig. 1. For the present study, we consider only conservative external forces, for which the total potential energy can be written as

$$\Pi = U - W \tag{1}$$

where W is the work done by conservative external forces. We can write strain energy and external work separately according to the 3D model and beam model,

$$\Pi = U_{3D} + U_{beam} - W_{3D} - W_{beam} - \left(W^I_{3D} + W^I_{beam}\right) \tag{2}$$

where W^I_{3D} and W^I_{beam} are internal work done by forces on the interface of the 3D part and the beam part, respectively. Forces on the interface are internal forces, but they can be viewed as external forces. For the 3D interface, the forces on the interface are reaction forces from the beam interface. For the beam interface, the forces are reaction forces from the 3D interface. One can thus write total potential energy as

$$\begin{aligned}\Pi = {} & \frac{1}{2}\int_{V_{3D}} \varepsilon\sigma \, dV_{3D} - \int_{S_u} u^{S_u} f^{S_u} \, dS_u - \int_{S_\sigma} u^{S_\sigma} f^{S_\sigma} \, dS_\sigma \\ & + \frac{1}{2}\int_{V_b} \varepsilon\sigma \, dV_b - \int_{S_{ub}} u^{S_{ub}} f^{S_{ub}} \, dS_{ub} - \int_{S_{\sigma_b}} u^{S_{\sigma_b}} f^{S_{\sigma_b}} \, dS_{\sigma_b} \\ & - \left(\int_{S_I} u^{S_I} f^{S_I} \, dS_I + \int_{S_{I_b}} u^{S_{I_b}} f^{S_{I_b}} \, dS_{I_b} \right)\end{aligned} \tag{3}$$

where S_u and S_{u_b} are the displacement boundaries of the 3D and beam models, respectively; S_σ and S_{σ_b} are the traction boundaries of the 3D and beam models, respectively; S_I and S_{I_b} are the traction boundaries, i.e., interface areas of the 3D and beam models, respectively; and u and f are displacement and tractions on the according displacement and traction boundary respectively. For simplicity, we assume that all displacement components on S_u and S_{u_b} are prescribed to be equal to zero. By writing the displacement field of each element in terms of nodal displacements and shape functions, integrating over each element, and taking the variation respect to nodal displacements, one can obtain the variation of total potential energy as

$$\begin{aligned}\delta\Pi = &\begin{bmatrix}\delta q_u^T & \delta q_I^T\end{bmatrix}\begin{bmatrix}K_{uu} & K_{uI}\\ K_{Iu} & K_{II}\end{bmatrix}\begin{Bmatrix}q_u\\ q_I\end{Bmatrix}+\begin{bmatrix}\delta\xi_I^T & \delta\xi_b^T\end{bmatrix}\begin{bmatrix}k_{II} & k_{Ib}\\ k_{bI} & k_{bb}\end{bmatrix}\begin{Bmatrix}\xi_I\\ \xi_b\end{Bmatrix}\\ &-\begin{bmatrix}\delta q_u^T & \delta q_I^T\end{bmatrix}\begin{Bmatrix}Q_u\\ Q_{I_e}\end{Bmatrix}-\delta\xi_b^T\,\Xi_b-\delta q_I^T\,Q_{I_i}-\delta\xi_I^T\,\Xi_I\end{aligned} \tag{4}$$

where $[K]$ is the stiffness matrix of the 3D solid model, $[k]$ is the stiffness matrix of the beam model, q is the nodal displacement of the 3D model, $\{\xi\}$ is the nodal displacement and rotations of the beam model, Q is the nodal forces of the 3D solid model, and $\{\Xi\}$ is the vector of sectional stress resultants of the beam model. The subscript u stands for the interior of the 3D model, I for the interface, and b for the beam interior. Specially Q_{I_e} and Q_{I_i} stand for the nodal forces on the interface from external loads and internal loads respectively.

The relationships between beam 1D displacements and rotations and the 3D displacement variables at the interface can be put in the form

$$R\,q_I = \xi_I \tag{5}$$

where R is a transformation matrix. Since R connects 3D nodal displacements with the beam displacements and rotation, R is called the transformation matrix from deflection continuity. The relationship between sectional stress resultants and the 3D nodal load over the section, when linearized, has the form

$$-S\,\Xi_I = Q_{I_i} \tag{6}$$

where S is a transformation matrix. Since S connects 3D nodal forces with the beam sectional stress resultants, S is called the transformation matrix from load continuity.

Substituting Eqs. (5) and (6) into the variation of total potential energy Eq. (4), and setting the variation to zero, leads to

$$\begin{bmatrix}K_{uu} & K_{uI} & 0\\ K_{Iu} & K_{II}+R^T k_{II} R & R^T k_{Ib}\\ 0 & k_{bI} R & k_{bb}\end{bmatrix}\begin{Bmatrix}q_u\\ q_I\\ \xi_b\end{Bmatrix}=\begin{Bmatrix}Q_u\\ Q_{I_e}\\ \Xi_b\end{Bmatrix}+\begin{Bmatrix}0\\ \left(R^T-S\right)\Xi_I\\ 0\end{Bmatrix} \tag{7}$$

where the last term on the right-hand side represents equilibrium on the interface which leads to

$$R^T = S \tag{8}$$

Therefore, we can use the transformation matrix from load continuity S instead of the deflection continuity transformation matrix R in the governing Eq. (7).

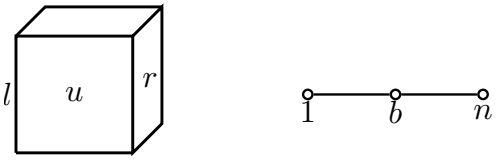

Figure 2: Base blocks - 3D and Beam model

For systems that include more than one 3D part and more than one beam part, the governing matrix can be assembled using base blocks shown in Fig. 2. In the base 3D block model, l stands for left interface, u for interior, and r for right interface. In the base beam block model, 1 is the left interface node, b stands for the interior nodes, and n for right interface node. The stiffness matrix for the base 3D block can be written as

$$K_{3D} = \begin{bmatrix} K_{ll} & K_{lu} & 0 \\ K_{ul} & K_{uu} & K_{ur} \\ 0 & K_{ru} & K_{rr} \end{bmatrix} \tag{9}$$

and the stiffness matrix for the base beam block can be written as

$$k_{beam} = \begin{bmatrix} S_1 k_{11} S_1^T & S_1 k_{1b} & 0 \\ k_{b1} S_1^T & k_{bb} & S_n k_{bn} \\ 0 & k_{nb} S_n^T & S_n k_{nn} S_n^T \end{bmatrix} \tag{10}$$

The assembly can be obtained by adding entries associated with beam interface nodes 1 or n to the corresponding 3D stiffness interface entries, K_{rr} or K_{ll}.

2.2 Dynamic formulation

Hamilton's principle in its most general form, usually referred to as Hamilton's extended principle, can be written as

$$\int_{t_1}^{t_2} \left[\delta (T - U) + \overline{\delta W} \right] dt = 0 \tag{11}$$

where T is the kinetic energy of the system, U is the strain energy of the system, $\overline{\delta W}$ is the work done by all external forces through a virtual displacement of the configuration, t is time, and t_1 and t_2 are arbitrary, fixed times. The kinetic energy T is

$$T = \frac{1}{2}\int_{V_{3D}} \rho\, \dot{u}^2\, dV_{3D} + \frac{1}{2}\int_{V_b} \rho\, \dot{u}^2\, dV_b \tag{12}$$

where ρ is the mass per unit volume, u is the displacement, $\dot{(\,)}$ is the first derivative with respect to time.

At the interface, the action and reaction forces are in equilibrium. Therefore, we can write

$$T = \frac{1}{2}\int_{V_{3D}} \rho\, \dot{u}^2\, dV_{3D} + \frac{1}{2}\int_{V_b} \rho\, \dot{u}^2\, dV_b - \left(\int_{S_I} \rho\, \ddot{u}\, dS_I + \int_{S_{I_b}} \rho\, \ddot{u}\, dS_{I_b}\right) \tag{13}$$

By using Eq. (5) in the kinetic expression, integrating in the time domain, and taking the variation with respect to displacements, we can obtain the mass matrix for the joined model with one 3D block and one beam block as,

$$\mathbf{M} = \begin{bmatrix} M_{uu} & M_{uI} & 0 \\ M_{Iu} & M_{II} + R^T m_{II} R & R^T m_{Ib} \\ 0 & m_{bI} R & m_{bb} \end{bmatrix} \tag{14}$$

where M is the mass matrix of the 3D model, m is the mass matrix of the beam model. If we write the stiffness matrix in Eq. (7) as $\mathbf{K}$, the free vibration of a simple joined problem can be written as

$$\mathbf{M}\ddot{u} + \mathbf{K}u = 0 \tag{15}$$

For joined models that include more than one 3D part and more than one beam part, the mass matrix can be assembled using the base blocks shown in Fig. 2. Similar to construction of the stiffness matrix, we can write the 3D base mass matrix as

$$M_{3D} = \begin{bmatrix} M_{ll} & M_{lu} & 0 \\ M_{ul} & M_{uu} & M_{ur} \\ 0 & M_{ru} & M_{rr} \end{bmatrix} \tag{16}$$

and the mass matrix for the base beam block can be written as

$$m_{beam} = \begin{bmatrix} S_1 m_{11} S_1^T & S_1 m_{1b} & 0 \\ m_{b1} S_1^T & m_{bb} & S_n m_{bn} \\ 0 & m_{nb} S_n^T & S_n m_{nn} S_n^T \end{bmatrix} \tag{17}$$

The assembly can be obtained by adding entries associated with beam interface nodes 1 or n to the corresponding 3D mass interface entries, M_{rr} or M_{ll}.

3 Transformation matrix S

We need to construct a transformation matrix S that leads to a relationship between the beam interface stress resultants and the 3D nodal loads over the interface. This relationship can be written as

$$\underline{F} = S\mathscr{F} \tag{18}$$

where $\underline{F}$ is the forces on nodes at 3D interface, and $\mathscr{F}$ is a column matrix of sectional stress resultants on the beam interface.

$$\begin{aligned} \underline{F} &= \begin{bmatrix} F_x^1 & F_y^1 & F_z^1 & \dots & F_x^n & F_y^n & F_z^n \end{bmatrix}^T \\ \mathscr{F} &= \begin{bmatrix} F_x & F_y & F_z & M_x & M_y & M_z \end{bmatrix}^T \end{aligned} \tag{19}$$

To construct matrix S stresses at the Gauss points are recovered first from the beam cross-sectional stress resultants. Then, the stresses at the Gauss points are regarded as normal distributed loads or surface tractions to form nodal concentrated loads. Stress recovery is discussed in section 3.1, and the formation of nodal loads is discussed in section 3.2.

3.1 Stress recovery

The relationship between beam sectional stress resultants and the generalized strain measures for the generalized Timoshenko beam model can be written as

$$\varepsilon = \Phi\mathscr{F} \tag{20}$$

where $\varepsilon = \begin{bmatrix} \gamma_{11} & 2\gamma_{12} & 2\gamma_{13} & \kappa_1 & \kappa_2 & \kappa_3 \end{bmatrix}^T$ are the generalized 1D strain measures obtained from a generalized Timoshenko beam analysis, $\mathscr{F}$ the cross sectional stress and moment resultants and Φ the 6×6 cross-sectional flexibility matrix which can be obtained from VABS constitutive analysis. Then, 1D strain measures for the generalized Timoshenko model can be rewritten as

$$\varepsilon = \begin{bmatrix} \gamma_{11} & \kappa_1 & \kappa_2 & \kappa_3 \end{bmatrix}^T \qquad \gamma_s = \begin{bmatrix} 2\gamma_{12} & 2\gamma_{13} \end{bmatrix}^T \tag{21}$$

Introducing permutation matrices P_I and P_J and using Eq. (20), we can write

$$\varepsilon = P_I\Phi\mathscr{F} \tag{22}$$

$$\gamma_s = P_J\Phi\mathscr{F} \tag{23}$$

with

$$P_I = \begin{bmatrix} 1 & 0 & 0 & 0 & 0 & 0 \\ 1 & 0 & 0 & 1 & 0 & 0 \\ 1 & 0 & 0 & 0 & 1 & 0 \\ 1 & 0 & 0 & 0 & 0 & 1 \end{bmatrix} \quad P_J = \begin{bmatrix} 0 & 1 & 0 & 0 & 0 & 0 \\ 0 & 0 & 1 & 0 & 0 & 0 \end{bmatrix} \tag{24}$$

Since P_I, P_J and Φ are constant matrices, we can differentiate both sides of Eqs. (22) and (23), and obtain

$$\begin{array}{ll} \varepsilon' = P_I \Phi \mathscr{F}' & \gamma_s' = P_J \Phi \mathscr{F}' \\ \varepsilon'' = P_I \Phi \mathscr{F}'' & \gamma_s'' = P_J \Phi \mathscr{F}'' \\ & \gamma_s''' = P_J \Phi \mathscr{F}''' \end{array} \tag{25}$$

We need to express the beam strain measures defined for the generalized Timoshenko model (ε and γ_s) in terms of the classical strain measures ($\bar{\varepsilon}$) used in the asymptotically correct model. The kinematical identity between these two sets of strain measures can be obtained as

$$\begin{aligned} \bar{\varepsilon} &= \varepsilon + Q\gamma_s' + P\gamma_s \\ \bar{\varepsilon}' &= \varepsilon' + Q\gamma_s'' + P\gamma_s' \\ \bar{\varepsilon}'' &= \varepsilon'' + Q\gamma_s''' + P\gamma_s'' \end{aligned} \tag{26}$$

with

$$Q = \begin{bmatrix} 0 & 0 \\ 0 & 0 \\ 0 & -1 \\ 1 & 0 \end{bmatrix} \quad P = \begin{bmatrix} 0 & 0 \\ k_2 & k_3 \\ -k_1 & 0 \\ 0 & -k_1 \end{bmatrix} \tag{27}$$

where the detailed derivation can be found in Hodges (2006).

To find the derivatives of the stress resultants, the 1D nonlinear equilibrium equations can be arranged as

$$\mathscr{F}' = -\mathscr{R} - \phi = -\begin{bmatrix} \widetilde{K} & O_3 \\ \widetilde{e_1} & \widetilde{K} \end{bmatrix} \mathscr{F} - \phi \tag{28}$$

where O_3 is a 3×3 matrix of zeros and the elements of ϕ are known distributed 1D applied and inertial forces and moments. For the present study, we consider zero distributed loads. One may discard the γ term in $\mathscr{R}$ by virtue of the small strain approximation. Therefore, higher derivatives of the stress resultants can be obtained as

$$\begin{aligned} \mathscr{F}'' &= \left(\mathscr{R}^2 - \mathscr{R}'\right) \mathscr{F} \\ \mathscr{F}''' &= \left(-\mathscr{R}^3 + \mathscr{R}\mathscr{R}' + 2\mathscr{R}'\mathscr{R} - \mathscr{R}''\right) \mathscr{F} \end{aligned} \tag{29}$$

Having $\mathscr{F}$, $\mathscr{F}'$, $\mathscr{F}''$ and $\mathscr{F}'''$, one can obtain ε, ε', ε'', γ_s, γ_s', γ_s'' and γ_s''' from Eqs. (22), (23) and (25). The strain measure $\bar{\varepsilon}$ and its derivatives can be obtained by substituting ε, γ_s and their derivatives into Eq. (26) as

$$\bar{\varepsilon} = C_{\bar{\varepsilon}} \mathscr{F}, \quad \bar{\varepsilon}' = C_{\bar{\varepsilon}'} \mathscr{F}, \quad \bar{\varepsilon}'' = C_{\bar{\varepsilon}''} \mathscr{F} \tag{30}$$

where

$$\begin{aligned} C_{\bar{\varepsilon}} &= P_I\Phi + PP_J\Phi - QP_J\Phi\mathscr{R} \\ C_{\bar{\varepsilon}'} &= QP_J\Phi(\mathscr{R}^2 - \mathscr{R}') - (P_I\Phi + PP_J\Phi)\mathscr{R} \\ C_{\bar{\varepsilon}''} &= (P_I + PP_j)\Phi(\mathscr{R}^2 - \mathscr{R}') + QP_J\Phi(-\mathscr{R}^3 + \mathscr{R}\mathscr{R}' + 2\mathscr{R}'\mathscr{R} - \mathscr{R}'') \end{aligned} \tag{31}$$

According to [Hodges (2006)], the 3D strain field can be recovered as follows

$$\begin{aligned} \Gamma = &[(\Gamma_a + \Gamma_R)(V_0 + V_{1R}) + \Gamma_\varepsilon]\bar{\varepsilon} \\ &+ [(\Gamma_a + \Gamma_R)V_{1S} + \Gamma_l(V_0 + V_{1R})]\bar{\varepsilon}' \\ &+ \Gamma_l V_{1S}\bar{\varepsilon}'' \end{aligned} \tag{32}$$

where the 3D strain field is defined in terms of column matrix

$$\Gamma = \begin{bmatrix} \Gamma_{11} & 2\Gamma_{12} & 2\Gamma_{13} & \Gamma_{22} & 2\Gamma_{23} & \Gamma_{33} \end{bmatrix}^T \tag{33}$$

and V_0, V_{1R} and V_{1S} are the nodal values of the asymptotically correct warping functions for classical modeling, the correction from nonzero initial curvatures/twist and the correction from transverse shear deformation, respectively. V_0, V_{1R} and V_{1S} can be obtained from the VABS cross-sectional analysis. The operators Γ_a, Γ_R, Γ_ε and Γ_l, which contain all the nodal coordinates and geometry information, are defined as

$$\Gamma_a = \begin{bmatrix} 0 & 0 & 0 \\ \frac{\partial}{\partial x_2} & 0 & 0 \\ \frac{\partial}{\partial x_3} & 0 & 0 \\ 0 & \frac{\partial}{\partial x_2} & 0 \\ 0 & \frac{\partial}{\partial x_3} & \frac{\partial}{\partial x_2} \\ 0 & 0 & \frac{\partial}{\partial x_3} \end{bmatrix} \tag{34}$$

$$\Gamma_\varepsilon = \frac{1}{\sqrt{g}} \begin{bmatrix} 1 & 0 & x_3 & -x_2 \\ 0 & -x_3 & 0 & 0 \\ 0 & x_2 & 0 & 0 \\ 0 & 0 & 0 & 0 \\ 0 & 0 & 0 & 0 \\ 0 & 0 & 0 & 0 \end{bmatrix} \tag{35}$$

$$\Gamma_R = \frac{1}{\sqrt{g}} \begin{bmatrix} \widetilde{k} + \Delta k_1 \left(x_3 \frac{\partial}{\partial x_2} - x_2 \frac{\partial}{\partial x_3} \right) \\ O_3 \end{bmatrix} \tag{36}$$

$$\Gamma_l = \frac{1}{\sqrt{g}} \begin{bmatrix} \Delta \\ O_3 \end{bmatrix} \tag{37}$$

where Δ is a 3×3 identity matrix, O_3 is a 3×3 matrix of zeros, the operator $\widetilde{(\ )}$ is defined such that $\widetilde{(\ )}_{ij} = -e_{ijk}(\ )_k$ and g is the determinant of the metric tensor for the undeformed state, with $\sqrt{g} = 1 - x_2 k_3 + x_3 k_2$.

For each element on the interface, the 3D strain Γ at a Gauss point can be obtained by knowing the coordinates of the Gauss point. In order to obtain the transformation matrix S, we need to write the 3D strain in terms of the sectional stress resultants $\mathscr{F}$. Substituting Eq. (30) into (32), we have

$$\Gamma = C_\Gamma \mathscr{F} \tag{38}$$

with

$$\begin{aligned} C_\Gamma = & \left[(\Gamma_a + \Gamma_R)(V_0 + V_{1R}) + \Gamma_\varepsilon \right] C_{\bar{\varepsilon}} \\ & + \left[(\Gamma_a + \Gamma_R) V_{1S} + \Gamma_l (V_0 + V_{1R}) \right] C_{\bar{\varepsilon}'} \\ & + \Gamma_l V_{1S} C_{\bar{\varepsilon}''} \end{aligned} \tag{39}$$

Therefore, the 3D stress field can be obtained using the 3D stress-strain relation, which is of the form

$$\sigma = \mathscr{D} \Gamma \tag{40}$$

where the 3D stress components are elements of the matrix

$$\sigma = \lfloor \ \sigma_{11} \quad \sigma_{12} \quad \sigma_{13} \quad \sigma_{22} \quad \sigma_{23} \quad \sigma_{33} \ \rfloor^T \tag{41}$$

and $\mathscr{D}$ is the 6×6 material matrix. In terms of sectional stress resultants, we can write the 3D stress field as

$$\sigma = \mathscr{D} C_\Gamma \mathscr{F} \tag{42}$$

3.2 Nodal load on interface

After we obtain the 3D stress field on the interface, the stresses at each Gauss point can be calculated given its coordinates. The stresses on the Gauss points in each element are regarded as normal force distribution or shear force distribution on the interface. Therefore, we can integrate the distributed load over the area surrounding the corresponding Gauss point and extrapolate the Gauss point forces to element nodes. By doing so over all the elements on the interface, we can obtain the nodal forces for all the nodes on the interface.

For brick elements, there are six stress components at each Gauss point: σ_{11}, σ_{12}, σ_{13}, σ_{22}, σ_{23}, and σ_{33}, as shown in Fig. 3. On the interface, the three components, σ_{11}, σ_{12}, σ_{13} can be regarded as surface tractions in the normal x_1 and tangential

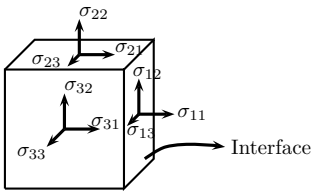

Figure 3: Stresses on an infinitesimal element at an arbitrary interface Gauss point

(i.e. shear) directions along x_2 and x_3, respectively. Therefore, the integration of σ_{11} gives the nodal force F_x in the x_1 direction, the integration of σ_{12} gives the nodal force F_y in the x_2 direction, and the integration of σ_{13} gives the nodal force F_z in the x_3 direction.

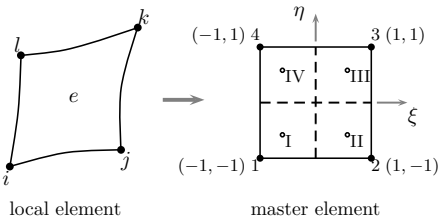

Figure 4: Gauss points on 2D four-noded master element

For an arbitrary 2D element e with four nodes, i, j, k, and l at the interface, we use four Gauss points denoted as I, II, III and IV in Fig. 4. We can integrate σ_{11}, σ_{12}, σ_{13} over the area surrounding the Gauss point to yield nodal forces F_x, F_y and F_z of the corresponding Gauss point. For example, at Gauss Point I in the master element, Gauss point forces can be calculated as

$$\begin{aligned} F_x^I &= \int_{-1}^{0}\int_{-1}^{0} \sigma_{11}^I |J|\, d\xi d\eta = \sigma_{11}^I A^I \\ F_y^I &= \int_{-1}^{0}\int_{-1}^{0} \sigma_{12}^I |J|\, d\xi d\eta = \sigma_{12}^I A^I \\ F_z^I &= \int_{-1}^{0}\int_{-1}^{0} \sigma_{13}^I |J|\, d\xi d\eta = \sigma_{13}^I A^I \end{aligned} \tag{43}$$

where $|J|$ is the determinant of the Jacobian matrix of the element e, and A^I is the area surrounding the Gauss point I. Then the nodal forces can be obtained by

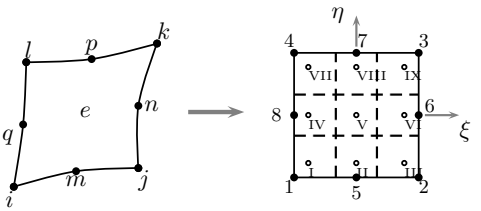

Figure 5: Gauss points on 2D eight-noded master element

extrapolation of the forces at Gauss points,

$$\begin{bmatrix} N_1(I) & N_2(I) & \cdots & N_m(I) \\ N_1(II) & N_2(II) & \cdots & N_m(II) \\ \vdots & \vdots & \vdots & \vdots \\ N_m(n) & N_m(n) & \cdots & N_m(n) \end{bmatrix} \begin{Bmatrix} F_i^1 \\ F_i^2 \\ \vdots \\ F_i^m \end{Bmatrix} = \begin{Bmatrix} F_i^I \\ F_i^{II} \\ \vdots \\ F_i^n \end{Bmatrix} \qquad (i = x, y, z) \tag{44}$$

where n is the total number of Gauss points, and m is the total number of element nodes. Therefore, the nodal forces can be obtained by solving the linear system of equations in Eqn. (44).

For an arbitrary 2D element e with eight nodes, i, j, k, l, m, n, p and q at the interface, we use nine Gauss points denoted as I, II, …, VIII, and IX in Fig. 5.

In the eight-noded element, there are nine Gauss integration points, the master element is partitioned into nine parts. The Gauss point forces, F_x, F_y and F_z, can be obtained by integrating σ_{11}, σ_{12}, σ_{13} over the area surrounding the Gauss point. For example, at Gauss Point I in the master element, the forces at that point can be calculated as

$$\begin{aligned} F_x^I &= \int_{-1}^{-\frac{1}{3}} \int_{-1}^{-\frac{1}{3}} \sigma_{11}^I |J| \, d\xi \, d\eta = \sigma_{11}^I A^I \\ F_y^I &= \int_{-1}^{-\frac{1}{3}} \int_{-1}^{-\frac{1}{3}} \sigma_{12}^I |J| \, d\xi \, d\eta = \sigma_{12}^I A^I \\ F_z^I &= \int_{-1}^{-\frac{1}{3}} \int_{-1}^{-\frac{1}{3}} \sigma_{13}^I |J| \, d\xi \, d\eta = \sigma_{13}^I A^I \end{aligned} \tag{45}$$

where $|J|$ is the determinant of the Jacobian matrix of the element e, and A^I is the area surrounding the Gauss point I.

Then the nodal forces at nodes i, j, k, l, m, n, p and q, if any, can be obtained by extrapolation of the forces at Gauss points using Eqn. (44). In a simplified form,

we can write

$$\underline{F^e} = P_A^e \, \sigma^e \tag{46}$$

where $\underline{F^e}$ is the vector of nodal forces in the element, P_A is a matrix including the area information of the element and shape function evaluated at the Gauss points, and σ^e is the vector of Gauss point stresses. Making use of Eq. (42), we have the relationship between element nodal forces and sectional stress resultants as

$$\underline{F^e} = P_A^e \, \mathscr{D}^e \, C_\Gamma^e \, \mathscr{F} \tag{47}$$

where the superscript e means these matrices are evaluated inside element e. So, we find the element transformation matrix S^e as

$$S^e = P_A^e \, \mathscr{D}^e \, C_\Gamma^e \tag{48}$$

For the whole interface, we can assemble the element transformation matrix S_e for every element on the interface to obtain the global transformation matrix S for this interface. Therefore, we can eliminate the superscripts and write

$$S = P_A \, \mathscr{D} \, C_\Gamma \tag{49}$$

4 Timoshenko Beam formulation

In this work, we consider a linear 1D generalized Timoshenko model for the beam formulation. Start with the kinematical equation subjected to any given boundary and loading conditions, and given the 1D stiffness matrix calculated by VABS

$$\begin{aligned} \gamma &= u' + \widetilde{k}\, u + \widetilde{e_1}\, \theta \\ \kappa &= \theta' + \widetilde{k}\, \theta \end{aligned} \tag{50}$$

where $u(x_1)$ is the column matrix of displacement measures expressed in the beam cross-sectional frame and $\theta(x_1)$ is the column matrix of infinitesimal cross-sectional rotations.

Using cubic beam shape functions N for four-noded beam element, we can write vector $u(x_1)$ and $\theta(x_1)$ in terms of shape functions, nodal displacements and rotations as

$$u = \sum_{i=1}^{n} N_i \, \underline{u}_i \quad \theta = \sum_{i=1}^{n} N_i \, \underline{\theta}_i \tag{51}$$

where

$$\underline{u}_i = \begin{Bmatrix} u_1^i \\ u_2^i \\ u_3^i \end{Bmatrix} \quad \underline{\theta}_i = \begin{Bmatrix} \theta_1^i \\ \theta_2^i \\ \theta_3^i \end{Bmatrix} \tag{52}$$

Substituting Eq. (52) into Eq. (50), we can write the kinematical equations in a simple matrix form

$$\left\{ \begin{array}{c} \gamma \\ \kappa \end{array} \right\} = dN \left\{ \begin{array}{c} \underline{u}_i \\ \underline{\theta}_i \end{array} \right\} \tag{53}$$

where dN is the $6 \times 6n$ matrix with n the number of nodes in the element, and has the form

$$dN = \begin{bmatrix} dN_1 & dN_2 & dN_3 & \cdots & dN_n \end{bmatrix} \tag{54}$$

with the components

$$dN_i = \begin{bmatrix} \frac{\partial N_i}{\partial x} & -k_3 N_i & k_2 N_i & 0 & 0 & 0 \\ k_3 N_i & \frac{\partial N_i}{\partial x} & -k_1 N_i & 0 & 0 & -N_i \\ -k_2 N_i & k_1 N_i & \frac{\partial N_i}{\partial x} & 0 & N_i & 0 \\ 0 & 0 & 0 & \frac{\partial N_i}{\partial x} & -k_3 N_i & k_2 N_i \\ 0 & 0 & 0 & k_3 N_i & \frac{\partial N_i}{\partial x} & -k_1 N_i \\ 0 & 0 & 0 & -k_2 N_i & k_1 N_i & \frac{\partial N_i}{\partial x} \end{bmatrix} \quad (i = 1, 2, \cdots, n) \tag{55}$$

The strain energy for the Timoshenko beam with constitutive law written in terms of generalized strains γ and κ can be expressed as

$$\mathscr{U} = \frac{1}{2} \int_0^l \left\{ \begin{array}{c} \gamma \\ \kappa \end{array} \right\}^T \mathscr{S} \left\{ \begin{array}{c} \gamma \\ \kappa \end{array} \right\} dx \tag{56}$$

where $\mathscr{S}$ is the 6×6 cross-sectional stiffness matrix which can be obtained from VABS cross-sectional constitutive analysis. Substituting the generalized strains in terms of nodal displacements and rotations, Eq. (53), into the energy equation, and taking the variation of the strain energy respect to nodal displacements and rotations, the element beam stiffness matrix k^e can be obtained as

$$k^e = \int_0^{l_e} dN^T \mathscr{S}\, dN\, dx \tag{57}$$

Considering a non-rotating linear beam problem, the kinetic energy of a beam can be written as

$$\mathscr{T} = \frac{1}{2} \int_0^l \left\{ \begin{array}{c} V \\ \Omega \end{array} \right\}^T \mathscr{M} \left\{ \begin{array}{c} V \\ \Omega \end{array} \right\} dx \tag{58}$$

where V and Ω are the velocities with $V = \dot{u}$ and $\Omega = \dot{\theta}$, and $\mathscr{M}$ is a cross-sectional mass matrix that can be obtained from the VABS cross-sectional analysis, and having the form

$$\mathscr{M} = \begin{bmatrix} \mu & 0 & 0 & 0 & \mu\bar{x}_3 & -\mu\bar{x}_2 \\ 0 & \mu & 0 & -\mu\bar{x}_3 & 0 & 0 \\ 0 & 0 & \mu & \mu\bar{x}_2 & 0 & 0 \\ 0 & -\mu\bar{x}_3 & \mu\bar{x}_2 & i_2+i_3 & 0 & 0 \\ \mu\bar{x}_3 & 0 & 0 & 0 & i_2 & i_{23} \\ -\mu\bar{x}_2 & 0 & 0 & 0 & i_{23} & i_3 \end{bmatrix} \tag{59}$$

where μ is the mass per unit length, $\bar{x}_2$ and $\bar{x}_3$ are offsets from the reference line of the cross-sectional mass centroid, and i_2, i_3 and i_{23} are cross-sectional mass moments and product of inertia. This matrix may also be written as

$$\mathscr{M} = \begin{bmatrix} \mu\Delta & -\mu\widetilde{\overline{\xi}} \\ \mu\widetilde{\overline{\xi}} & i \end{bmatrix} \tag{60}$$

where $\overline{\xi} = \begin{bmatrix} 0 & \bar{x}_2 & \bar{x}_3 \end{bmatrix}^T$

Hamilton's principle for this linear non-rotating free-vibration beam problem can be written as

$$\int_{t_1}^{t_2} \left[\delta\left(\mathscr{T} - \mathscr{U}\right)\right] = 0 \tag{61}$$

Substituting strain energy and kinetic energy into this equation, integrating the resulting expression by parts to bring u and θ into evidence, we can obtain the governing equation for free vibration of this beam problem

$$m \begin{Bmatrix} \ddot{\underline{u}}_i \\ \ddot{\underline{\theta}}_i \end{Bmatrix} + k \begin{Bmatrix} \underline{u}_i \\ \underline{\theta}_i \end{Bmatrix} = 0 \tag{62}$$

where m is the beam mass matrix, and k is the beam stiffness matrix. The element beam mass matrix has the form

$$m^e = \int_0^{l^e} N^T \mathscr{M} N \, dx \tag{63}$$

where N is a $6 \times 6n$ matrix with N_i the shape functions and Δ the 6×6 identity matrix.

$$N = \begin{bmatrix} N_1\Delta & N_2\Delta & N_3\Delta & \cdots & N_n\Delta \end{bmatrix} \tag{64}$$

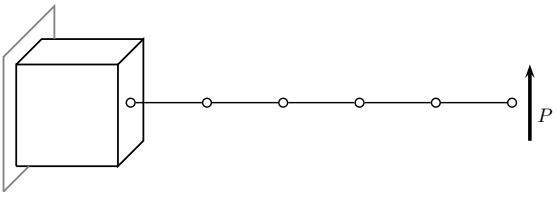

Figure 6: Joined 3D-beam example

5 Joined 3D-beam Examples

5.1 Static Response

For the joined 3D-beam problem, we consider first a simple example shown in Fig. 6. The structure is clamped at the left end and subjected to a shear force (1000 N) at the right end. Since the beam model cannot capture the details of the structure root, the clamped end is modeled as a 3D model, and the rest of the structure is modeled as a beam. Fig. 6 shows the configuration of this joined structure. The geometry and material properties of the structure are given in Table 1.

Table 1: Dimensions and properties of the joined 3D-beam structure

Dimensions
Total length = 12 m
Length of the 3D part = 1 m
Length of the beam part = 11 m
Height $2b$ = 1 m
Thickness t = 0.5 m
Material properties
E = 70 GPa
ν = 0.35
ρ = 2750 kg/m^3

5.1.1 Convergence of displacement for static problem

To examine the convergence of the joined 3D-beam analysis, cases are performed using different numbers of 3D elements with the number of beam elements kept

the same. For the joined models in this section, the 3D parts are constructed with various numbers of 20-noded elements, and the beam parts are constructed with 13 four-noded elements.

In order to verify the results of the joined models, full 3D analyses are preformed using ABAQUS 6.8. For each joined 3D-beam model, a corresponding full 3D ABAQUS model with the same mesh density model is analyzed. By saying the mesh densities are the same, we mean the mesh density in the full 3D model is the same as that of the 3D part in the joined model. Results obtained from the ABAQUS models are compared with those from the joined models. The transverse displacement for the full 3D model is evaluated at the center of the right end cross section.

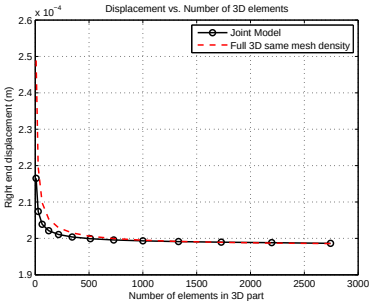

Figure 7: Right end transverse displacement u_2 vs. the number of 3D elements used in joined 3D-beam model

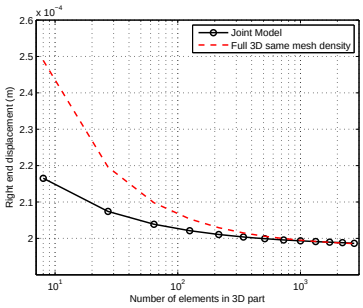

Figure 8: Right end u_2 vs. number of 3D elements used in joined 3D-beam model on a logarithmic scale

Figure 7 shows the right-end u_2 from the joined 3D-beam and ABAQUS analyses, versus the number of 3D elements used in the joined 3D-beam model. For a clearer view, Fig. 8 shows the same results on a logarithmic scale. From Figs. 7 and 8, one can observe that the displacement converges as the number of 3D elements increases. Compared to the full 3D results, the joined 3D-beam results converge to approximately the same point. When the number of 3D elements is small, the convergence rate is low. When the number of 3D elements is larger, the results converge faster. For the same mesh density models, the CPU time of the joined model, shown in Table 2 is much less than that of the full 3D model. The example shows the methodology we have established as a proof of concept. Unfortunately, we were hindered by the linear solver we chose and did not obtain a significant gain in computational efficiency. It is clear, however, that this can be improved in our planned future work, once we (a) use a commercial code for the 3D elements and (b) use a linear solver that is suitable for use with commercial codes.

Table 2: CPU time for static analysis for joined 3D-beam and full ABAQUS 3D models

Number of Elements in 3D part	ABAQUS with same mesh density (s)	Joined 3D-beam (s)
8	1	0.04
27	1	0.12
64	3	0.35
125	5	1
216	9	2.5
343	17	5
512	30	11
729	60	23
1000	92	45
1331	156	96
1728	337	161
2197	441	264
2744	620	402

5.1.2 Convergence of load continuity

In this section, we will examine the effect of interface mesh density on load continuity. Suppose we apply 1000 N for sectional stress resultants, F_x, F_y, F_z, and 1000 N·m for sectional moment resultants M_x, M_y, and M_z, at the interface. After the recovery process, we can obtain all nodal forces at the interface. Then, sectional stress resultants are calculated using these recovered nodal forces. Fig. 9 shows the convergence trend for recovered sectional stress resultants at the interface for different interface meshes.

From Fig. 9, one can observe that the recovered sectional stress resultants converge to applied loads when the number of interface elements increases. Among these six sectional stress and moment resultants, F_x, F_y, F_z, M_x, M_y, and M_z, the axial force converges the fastest and the torque M_x the slowest. When there is an insufficient number of interface elements, the recovered sectional stress resultants are inaccurate, making the interface load continuity inaccurate. This accounts for the relatively large difference between results from the joined 3D-beam and full 3D analyses, when the number of 3D elements is small.

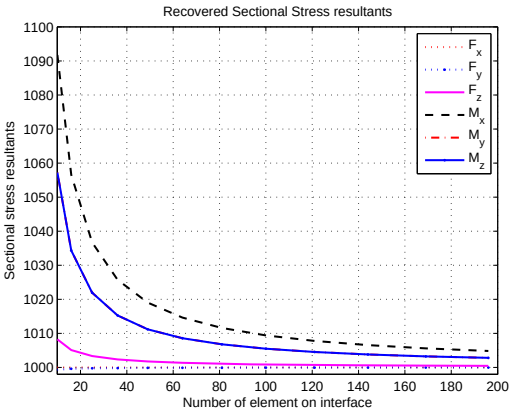

Figure 9: Recovered interface sectional stress resultants for different interface mesh

5.1.3 Strains and stresses at a sample cross section

In order to verify the credibility of the joined 3D-beam static analysis, a sample cross section is selected at $x = 0.5$, where results obtained for the major strains and stresses are compared between those of the joined 3D-beam method and of a full ABAQUS 3D model with same mesh density. For the joined 3D-beam models, 1,728 20-noded elements are used in the 3D part. For the full ABAQUS 3D method, 20,736 20-noded elements are used. There are 144 elements at the interface.

Figures 10 and 11 show the normal strain ε_{11} and shear strain ε_{12} distribution on the sample cross section, respectively. From Fig. 10 one can observe that the normal strain ε_{11} distribution for the joined 3D-beam model agrees quite well with that from a full 3D analysis, and within the precision of the plot differences are not noticeable. From Fig. 11 one can observe that the shear strain ε_{12} distribution on the sample cross section for the joined 3D-beam model also agrees well with that from the full 3D analysis. For a clearer view of the magnitude of the strains, Fig. 12 shows the comparison between normal strain ε_{11} distribution along the line $x = 0.5,\ z = 0$ for the joined 3D-beam model and the full 3D analysis. Figure 13 shows the comparison between shear strain ε_{12} distribution along the same line for both analysis. From Fig. 12 and 13, one can observe that in the close up view, normal strain ε_{11} from the joined 3D-beam analysis agrees very well with the full ABAQUS 3D analysis, and there is no visible difference within the precision of the plot. The shear strain ε_{12} from the joined 3D-beam analysis also agrees well with full ABAQUS 3D analysis, though one can detect a very slight difference between

the two curves.

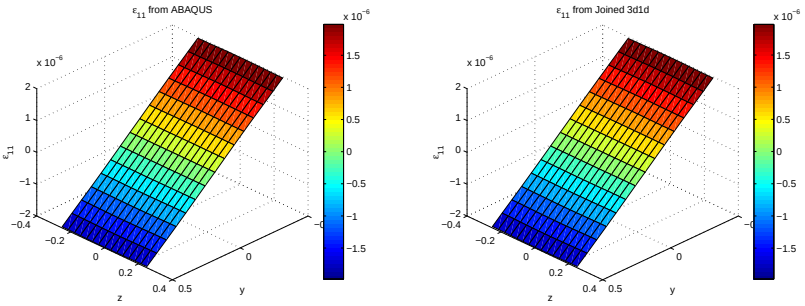

(a) ε_{11} from ABAQUS (b) ε_{11} from joined model

Figure 10: Normal strain ε_{11} distribution on sample cross section

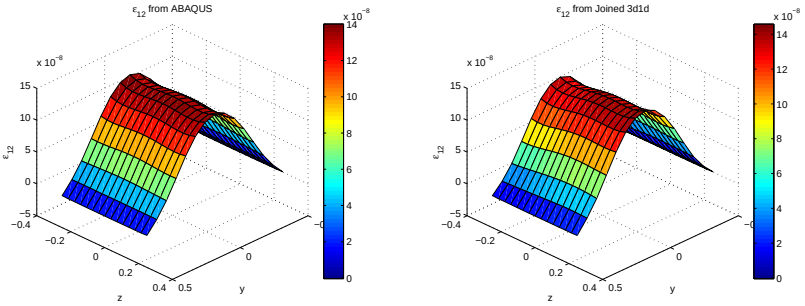

(a) ε_{12} from ABAQUS (b) ε_{12} from joined model

Figure 11: Shear strain ε_{12} distribution on sample cross section

Figures 14 and 15 show the normal stress σ_{11} and shear stress σ_{12} distribution on the sample cross section, respectively. From Fig. 14 one can observe that the normal stress σ_{11} distribution on the sample cross section for the joined 3D-beam model agrees really well with full 3D analysis, and one can hardly detect any differences within the precision of the plot. From Fig. 15 one can observe that the shear stress σ_{12} distribution on the sample cross section for the joined 3D-beam model agrees well with the full 3D analysis.

For a clearer view of the magnitude of the stresses, Fig. 16 shows the comparison of normal strain σ_{11} distribution along the line $x = 0.5$, $z = 0$ for the joined 3D-beam and full 3D analysis. Figure 17 shows the comparison of shear stress σ_{12} distribution along the same line for both analysis. From Figs. 16 and 17, one can

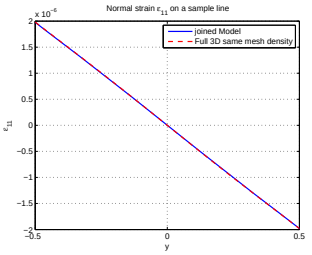

Figure 12: Normal strain ε_{11} distribution along the line $x = 0.5,\ z = 0$

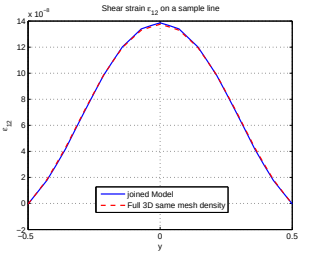

Figure 13: Shear strain ε_{12} distribution along the line $x = 0.5,\ z = 0$

observe in the close-up view that the normal stress σ_{11} from the joined 3D-beam analysis agrees very well with the full ABAQUS 3D analysis, and there is no visible difference within the plot precision. For the shear stress σ_{12}, the joined 3D-beam analysis also agrees well with full ABAQUS 3D analysis, though there is a slight difference between the two curves.

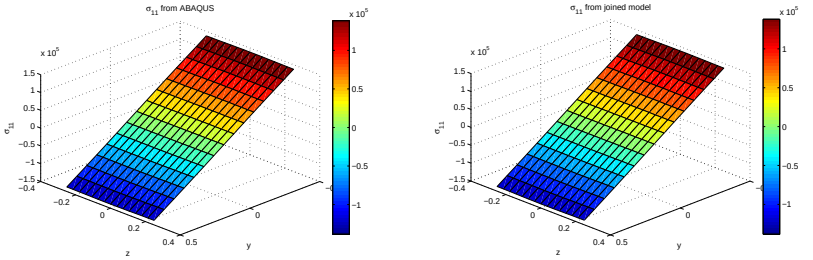

(a) σ_{11} from ABAQUS (b) σ_{11} from joined model

Figure 14: Normal stress σ_{11} distribution on sample cross section

The above static analysis of a simple beam example shows that the joined 3D-beam method successfully captures the response of the beam model and gives reliable results for displacement, strain and stress with less computation time.

5.2 Free-Vibration Frequencies

For the same model as shown in Fig. 6 but without the right-end shear force and with properties as specified in Table 1, the free-vibration frequencies are examined for various cases that use different numbers of 3D elements but with the number of beam elements kept the same. For all the joined models, the 3D parts are

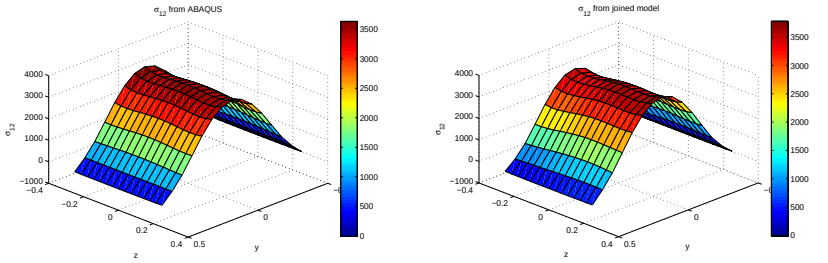

(a) σ_{12} from ABAQUS (b) σ_{12} from joined model

Figure 15: Shear stress σ_{12} distribution on sample cross section

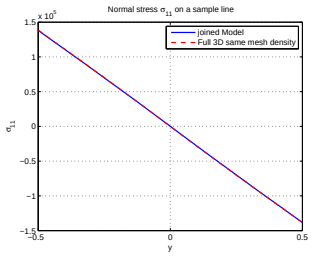

Figure 16: Normal stress σ_{11} distribution along the line $x = 0.5,\ z = 0$

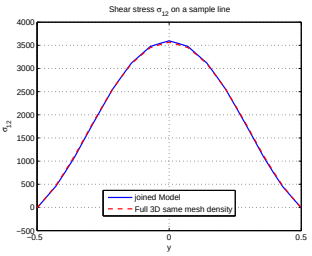

Figure 17: Shear stress σ_{12} distribution along the line $x = 0.5,\ z = 0$

constructed with various numbers of 20-noded elements, and the beam parts are constructed with 13 four-noded elements.

Results from the joined 3D-beam models are compared with those for a full ABAQUS 3D model having the same mesh density as the 3D part of the joined model. For both joined 3D-beam and full ABAQUS 3D analysis, we computed the lowest fourteen frequencies.

Figure 18 shows the normalized frequencies versus the number of 3D elements in the joined model. The frequencies are normalized by those of the full 3D fine mesh results. For a clearer view, Fig. 19 shows the same results on a logarithmic scale. From Figs. 18 and 19, one can observe that the normalized frequencies approach to unity as the number of 3D elements increases, which means the frequencies from joined 3D-beam model converge to the 3D fine mesh results. The computation time, listed in Table 3, for the free-vibration analysis for the joined 3D-beam method is less than that of full ABAQUS 3D analysis, since we used far fewer elements in the joined 3D-beam model. For models with a larger number of 3D elements, the advantage of the joined 3D-beam model is more obvious. As stated before, the

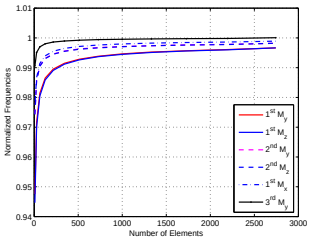

Figure 18: Normalized frequencies vs. number of 3D elements

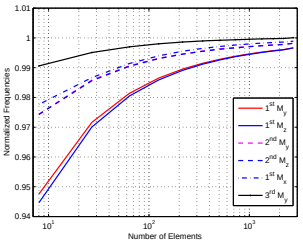

Figure 19: Frequencies vs. number of 3D elements on a logarithmic scale

computation will be much more efficient when a more efficient linear equation solver is used in the code.

The free-vibration analysis of this simple beam example shows that the joined 3D-beam method gives reliable results for the natural frequencies with less computation time than the full 3D analysis. The full 3D analysis, however, involves far more possible boundary conditions, and this effect is next considered.

5.3 Effect of Various Boundary Constraints

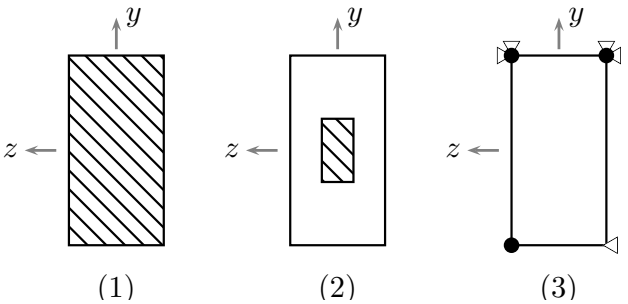

Figure 20: Three cases of boundary constraints at the root cross section

A beam model can only be constrained in terms of its 1D variables, which typically are averaged displacements and rotations over the section. However, the joined 3D-beam model and full 3D models are capable of analyzing static or dynamic beam-like models with a huge variety of boundary conditions by constraining various combinations of nodal displacements over a boundary cross section. *No beam model capture these effects*. To test the efficacy of the approach, three cases of root

Table 3: CPU time for free-vibration analysis of joined 3D-beam and full ABAQUS 3D models

Number of Elements in 3D part	Joint 3D-beam (s)	ABAQUS with same mesh density (s)
8	0.15	1
27	0.4	2
64	1.6	4
125	3.5	10
216	10	21
343	23	36
512	57	65
729	96	117
1000	198	241
1728	900	1590
2197	1199	2367
2744	2053	4040

end boundary constraints, shown in Fig. 20, are examined using joined 3D-beam and full ABAQUS 3D analyses. The first case is to constrain all the nodal displacements (u_x, u_y, u_z) at the root cross section. The second case is to constrain the nodal displacements (u_x, u_y, u_z) at a core region of the root cross section. The third case is to only constrain nodal displacements to be zero at the corners of the root cross section, with constrains on u_x, u_y, u_z at the two upper corner nodes, u_x at the bottom left corner node, and u_z at the bottom right corner node.

Figure 21 shows the variation of frequencies for the three different boundary constraints using the full ABAQUS 3D analysis and the joined 3D-beam analysis, respectively. From Fig. 21, one can observe that the natural frequencies become higher when more degrees of freedom are constrained at the boundary. Case one has the highest natural frequencies, and case three has the lowest natural frequencies. From Fig. 21, one can observe that the joined 3D-beam models successfully capture the changes of frequency caused by the various boundary constraints. From this figure, one can observe that the frequencies from the joined 3D-beam models agree very well with the full ABAQUS 3D analysis at low modes. For higher modes, such as 6^{th} M_y, there are differences between results for the joined 3D-beam and full 3D, but the joined model is still a good approximation.

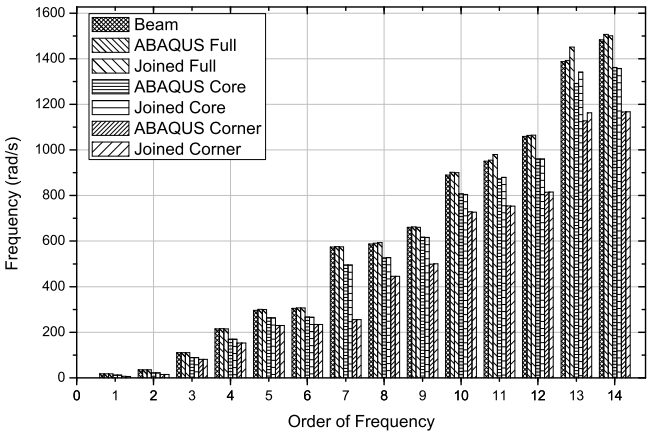

Figure 21: Frequencies for different boundary conditions using full ABAQUS 3D analysis and joined 3D-beam analysis

Figure 21 also shows the frequencies from pure beam analysis. One can observe that the pure beam analysis is a good approximation to full 3D analysis with full end constraint, but a pure beam analysis cannot approximate the effects of a partly constrained boundary at the root section. Because only averaged displacements and rotations can be constrained at a boundary in a beam analysis, analyses cannot capture the changes of frequency caused by various boundary conditions.

The examples in this section show that the joined 3D-beam method can successfully capture the frequency change caused by various boundary constraints, which pure beam analyses cannot achieve. This can be done far more efficiently than can a full 3D analysis.

5.4 Nonuniform Beam Example

[Hodges, Ho, and Yu (2008)] demonstrated that traditional beam models cannot recover accurately the stress and strain distributions in the vicinity of spanwise nonuniformities because the standard cross-sectional analysis does not take into account the effect of spanwise uniformity on the lateral surface boundary conditions. To take into account even such a simple effect as linear taper results in very complicated cross-sectional analysis, altered boundary conditions on the lateral surface of the beam, altered elastic constants and altered stress/strain recovery relations. In what follows, when we mention the inadequacies of stress or strain recovery

from beam theory, we are talking about recovery relations based on cross-sectional analysis for spanwise uniform beams (such as the theory embodied in VABS).

However, by using a joined 3D-beam model, a nonuniform beam can be analyzed by separating the original model into several parts. The uniform parts can be modeled as uniform beams, and the nonuniform parts can be modeled as 3D solid models. In this section, free-vibration of the nonuniform beam structure shown in Fig. 22 is analyzed using full ABAQUS 3D and joined 3D-beam models. For the joined 3D-beam model, shown in Fig. 23, the root end and the nonuniform part are constructed as 3D models, and the uniform parts are modeled as beams.

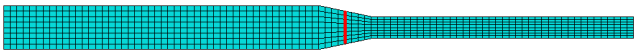

Figure 22: Nonuniform beam structure modeled using ABAQUS, X-Y view

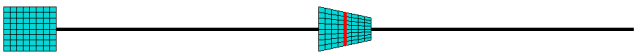

Figure 23: Nonuniform beam structure modeled using joined 3D-beam model, X-Y view

Figure 23 shows the nonuniform beam. For the static analysis, the beam is clamped at the left end and the free right end subject to an applied shear force of 1,000 N. For the free-vibration analysis, the beam is clamped at the left end. The length of the larger cross section part is six meters, and the length of the smaller cross section part is five meters. The length of the nonuniform part is one meter. The larger cross section is one meter high and a half-meter deep, and the smaller cross section is a half-meter square. The material properties are the same as in Table 1.

5.4.1 Frequencies

Figure 24 shows the frequencies for this nonuniform beam using joined 3D-beam and full ABAQUS 3D models. For the joined 3D-beam model, 512 20-noded elements are used in each 3D part. For a full ABAQUS full model with the same mesh density, 6,144 20-noded elements are used. For a full ABAQUS 3D model with fine mesh, 33,740 20-noded elements are used. From Fig. 24, one can observe that the frequencies from the joined 3D-beam analysis agree very well with those from

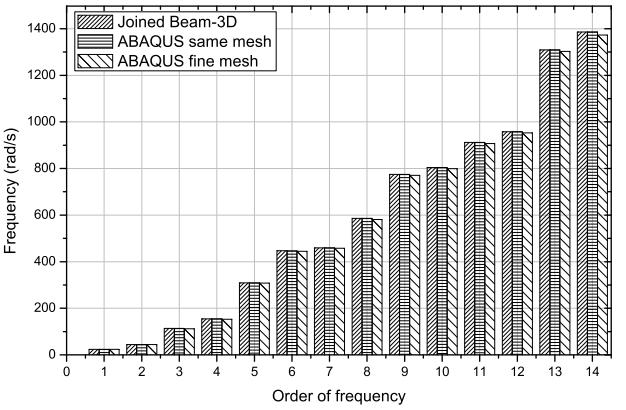

Figure 24: Frequencies for nonuniform beam model using joined 3D-beam and ABAQUS 3D analyses

the full ABAQUS 3D analysis. The relative errors are quite small, demonstrating that the joined 3D-beam model is an efficient but very good approximation of a full 3D analysis.

5.4.2 Strains and stresses

A sample cross section is selected at $x = 6.5$, which is the mid-section of the nonuniform block. The strains and stresses on that sample section from the joined 3D-beam method are compared with a full ABAQUS 3D model with same mesh density. We also computed the strains using beam analysis with VABS strain recovery. In order to use VABS recovery, a beam analysis is carried out using ABAQUS. Beam displacements and rotations at the sample cross section are obtained. In the ABAQUS beam modeling, sixteen beam elements are used in the nonuniform part. Different cross sections are defined and associated to the beam elements in the nonuniform part.

Figures 25 and 26 show the normal strain ε_{11} and shear strain ε_{12} distribution on the sample cross section, respectively. From Fig. 25 one can observe that the normal strain ε_{11} distribution on the sample cross section for the joined 3D-beam model agrees really well with that for the full 3D analysis, and no differences are observed within the precision of the plot. From Fig. 25(c), one can observe that the results obtained from strain recovery based on beam theory are almost an order of magnitude higher than for the full 3D analysis. Therefore, standard beam analysis

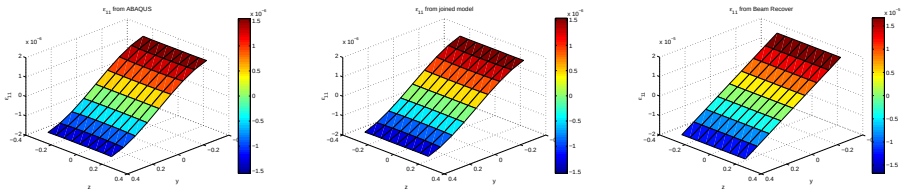

(a) ε_{11} from ABAQUS (b) ε_{11} from joined model (c) ε_{11} from beam recovery

Figure 25: Normal strain ε_{11} distribution on sample cross section

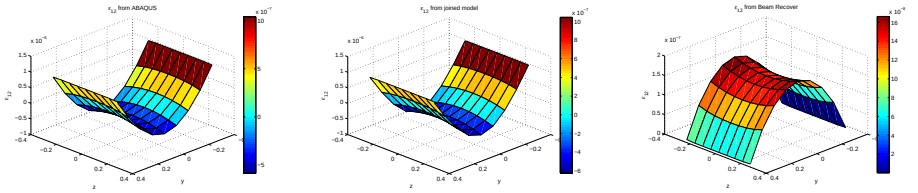

(a) ε_{12} from ABAQUS (b) ε_{12} from joined model (c) ε_{12} from beam recovery

Figure 26: Shear strain ε_{12} distribution on sample cross section

gives unrealistic results and is therefore not applicable to this nonuniform beam problem. From Fig. 26 one can observe that the shear strain ε_{12} distribution on the sample cross section for the joined 3D-beam model agrees very well with that from the full 3D analysis, but the shear strain from beam theory is totally different; therefore, beam analysis with strain recovery cannot be used to obtain strain distributions in the vicinity of a spanwise nonuniformity in a beam problem.

For a clearer view of the magnitude of the strains, Fig. 27 shows the comparison between normal strain ε_{11} distribution along the line $x = 6.5$, $z = 0$ for full 3D, joined 3D-beam analysis, and recovery based on beam theory. Figure 28 shows the comparison between shear strain ε_{12} distribution along the line $x = 6.5$, $z = 0$ for full 3D, joined 3D-beam analysis, and recovery based on beam theory. From Figs. 27 and 28, in the close-up view one can observe that the normal strain ε_{11} from the joined 3D-beam analysis agrees very well with the full ABAQUS 3D analysis, and there is no visible difference within the plot precision. For the shear strain ε_{12}, the joined 3D-beam analysis agrees very well with full ABAQUS 3D analysis with a little difference at $y = 0$.

For a uniform, clamped-free beam with rectangular cross section, subjected to a shear force at the free end, classical beam theory indicates that the shear strain distribution is a parabola. The surface tractions on the upper and bottom surfaces of each cross section are zero. However, when there is spanwise nonuniformity, the

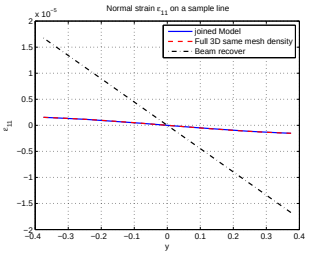

Figure 27: Normal strain ε_{11} distribution along the line $x = 6.5,\ z = 0$

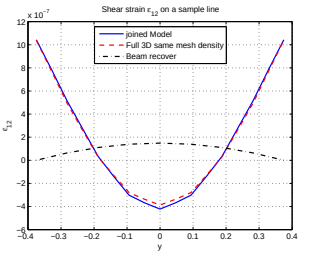

Figure 28: Shear strain ε_{12} distribution along the line $x = 6.5,\ z = 0$

parabolic shear stain distribution is no longer correct, and those stresses no longer vanish on the boundary Hodges, Ho, and Yu (2008). Overall, the joined 3D-beam analysis gives good results compared with those of the full ABAQUS 3D analysis, but the recovery results based on beam theory are not at all accurate.

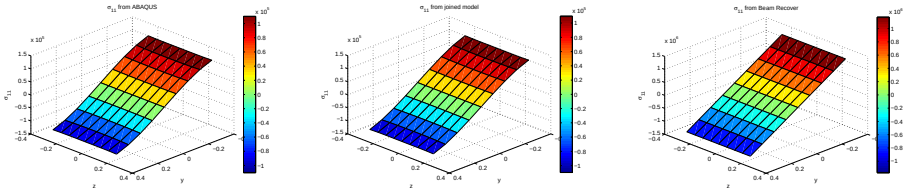

(a) σ_{11} from ABAQUS (b) σ_{11} from joined model (c) σ_{11} from beam recovery

Figure 29: Normal stress σ_{11} distribution on sample cross section

Figures 29 and 30 show the normal stress σ_{11} and shear stress σ_{12} distributions, respectively, on the sample cross section. From Fig. 29 one can observe that the normal stress σ_{11} distribution on the sample cross section for the joined 3D-beam model agrees really well that from the full 3D analysis, and differences are not noticeable within the precision of the plot. However, Fig. 25(c) gives stresses that are almost one order of magnitude higher than those obtained from the full 3D analysis. Therefore, beam analysis with VABS stress recovery, which is asymptotically exact for spanwise uniform beams, is not suitable for solving this nonuniform beam problem, since it gives unrealistic results. From Fig. 30 one can observe that the shear stress σ_{12} distribution on the sample cross section for the joined 3D-beam model agrees well with full 3D analysis, but shear stresses from stress recovery based on beam theory are totally different from the other two. Therefore, beam analysis with stress recovery based on the assumption of uniformity cannot be used

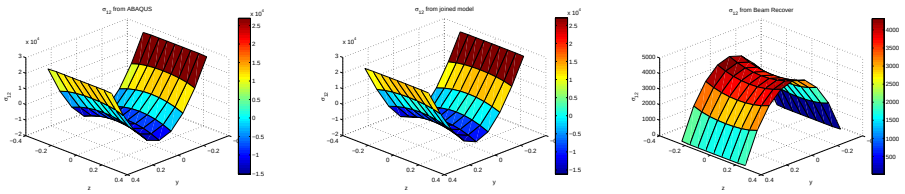

(a) σ_{12} from ABAQUS (b) σ_{12} from joined model (c) σ_{12} from beam recovery

Figure 30: Shear stress σ_{12} distribution on sample cross section

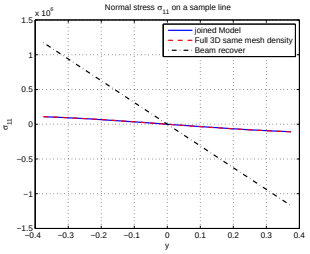

Figure 31: Normal stress σ_{11} distribution along the line $x = 6.5,\ z = 0$

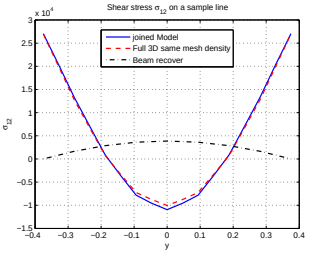

Figure 32: Shear stress σ_{12} distribution along the line $x = 6.5,\ z = 0$

to recover stresses in a spanwise nonuniform beam.

For a clearer view of the magnitude of the stresses, Fig. 31 shows the comparison of normal stress σ_{11} distribution along the line $x = 6.5,\ z = 0$ for full 3D, joined 3D-beam analysis, and stress recovery from beam theory. Figure 32 shows the comparison of shear stress σ_{12} distribution along the line $x = 6.5,\ z = 0$ for full 3D, joined 3D-beam analysis, and stress recovery from beam theory. From Figs. 31 and 32, one can observe that in the close up view, normal stress σ_{11} from the joined 3D-beam analysis agrees very well with the full ABAQUS 3D analysis, and there is no visible difference within the plot precision. For the shear stress σ_{12}, the joined 3D-beam analysis agrees very well with full ABAQUS 3D analysis with a little difference at $y = 0$. Overall, the joined 3D-beam analysis gives good results to compare with the full ABAQUS 3D analysis, but the results obtained from stress recovery based on beam theory are inaccurate.

The nonuniform beam example shown in this section shows that the joined 3D-beam approach successfully captures the response of a nonuniform beam-like structure and gives reliable results. But pure beam analysis with stress and strain recovery based on cross-sectional analysis developed for spanwise uniform beams cannot give accurate results.

6 Conclusions

The current paper presents a rigorous and consistent approach to construct a finite element analysis that joins 3D solid models to beam models. The approach uses asymptotically reduced beam models over all beam-like parts of a complex structure away from boundaries and away from points of discontinuity along the span in geometry or materials. 3D finite elements are used to model other parts of the structure for which beam models are inaccurate. The reduced model and the 3D model are assembled together to obtain the solution. The asymptotically correct warping functions at the interface are used to construct a transformation matrix, which makes the current method more accurate than existing transition element methods.

Four examples provided in the paper show that the joined 3D-beam approach successfully captures the static response and free-vibration frequencies with less computation time than a 3D model, while also capturing the frequency changes caused by different boundary constraints, which beam analyses cannot capture. The joined 3D-beam approach also can capture accurately the stresses and strains of a spanwise nonuniform beam-like structure, whereas a beam analysis with strain or stress recovery does not provide accurate results. The presented approach also gives accurate results for problems such as finding the effects of 3D constraints at beam boundaries. In such cases pure beam models give inaccurate results. Finally, the joined 3D-beam approach greatly reduces the computation time compared to full 3D analysis.

Therefore, the joined 3D-beam approach successfully couples the disparate finite element types into a single finite element model making use of the asymptotically exact information available in reduced-dimensional models based on variational-asymptotic theory (such as beam analysis using elastic constants from VABS). Using this approach, a complex structure can be analyzed by making maximum use of simplified models without the loss of accuracy presently incurred in dimensionally-reduced models near boundaries or where joined to inherently 3D structures. The methodology used to form joined 3D-beam approach can also be applied to joining other types of elements in the future. Although the current examples are linear isotropic models, the method can be extended to nonlinear, composite beam-like models. A composite example is not yet available because of the constraint imposed by the solver used; in particular, the current solver cannot solve linear systems with a large number of degrees of freedom. In planned future work the code will be modified so as to make use of a better solver and thereby obtain much greater computational efficiency.

References

Abel, J. F.; Shephard, M. S. (1979): An algorithm for multipoint constraints in finite element analysis. *International Journal for Numerical Methods in Engineering*, vol. 14, pp. 464–467.

Ahn, J. S.; Basu, P. K. (2011): Locally refined p-fem modeling of patch repaired plates. *Composite Structures*, vol. 93, pp. 1704–1716.

Aminpour, M. A.; Krishnamurthy, T. (1997): A two-dimensional interface element for multi-domain analysis of independently modelled three-dimensional finite element meshes. In *Presented at the AIAA/ASME/ASCE/AHS/ASC 38th Structures, Structural Dynamics and Materials Conference, Kissimmee, FL.*

Aminpour, M. A.; Ransom, J. B.; McCleary, S. L. (1992): Coupled analysis of independently modelled finite element subdomains. In *AIAA/ASME/ASCE/AHS/ASC 33rd Structures, Structural Dynamics, and Materials Conference, Dallas, TX.*

Aminpour, M. A.; Ransom, J. B.; McCleary, S. L. (1995): A coupled analysis method for structures with independently modelled finite element subdomains. *International Journal for Numerical Methods in Engineering*, vol. 38, pp. 3695–3718.

Avdeev, I. V.; Borovkov, A. I.; Kiylo, O. L.; Lovell, M. R.; Jr, D. O. (2002): Mixed 2d and beam formulation for modeling sandwich structures. *Engineering Computations*, vol. 19, pp. 451–466.

Berdichevskii, V. L. (1979): Variational-asymptotic method of constructing a theory of shells. *PMM Journal of Applied Mathematics and Mechanics*, vol. 43, pp. 664–687.

Chavan, K. S.; Wriggers, P. (2004): Consistent coupling of beam and shell models for thermo-elastic analysis. *International Journal For Numerical Methods In Engineering*, vol. 59, pp. 1861–1878.

Chung, W.; Sotelino, E. D. (2006): Three-dimensional finite element modeling of composite girder bridges. *Engineering Structures*, vol. 28, pp. 63–71.

Cofer, W. F.; Will, K. M. (1991): A three-dimensional, shell-solid transition element for general nonlinear analysis. *Computers and Strucrures*, vol. 38, pp. 449–462.

Curiskis, J. I.; Valliappan, S. (1978): A solution algorithm for linear constraint equations in finite element analysis. *Computers and Strucrures*, vol. 8, pp. 117–124.

Davila, C. G. (1994): Solid-to-shell transition elements for the computation of interlaminar stresses. *Computing Systems in Engineering*, vol. 5, pp. 193–202.

Dohrmann, C. R.; Key, S. W. (1999): A transition element for uniform strain hexahedral and tetrahedral finite elements. *International Journal for Numerical Methods in Engineering*, vol. 44, pp. 1933–1950.

Dohrmann, C. R.; Key, S. W.; Heinstein, M. W. (2000): Methods for connecting dissimilar three-dimensional finite element meshes. *International Journal for Numerical Methods in Engineering*, vol. 47, pp. 1057–1080.

E.Wyart, D.Coulon, T. J. R.; F.Lani (2009): Application of the substructured finite element/extended finite element method (s-fe/xfe) to the analysis of cracks in aircraft thin walled structures. *Engineering Fracture Mechanics*, vol. 76, pp. 44–58.

Garusi, E.; Tralli, A. (2002): A hybrid stress-assumed transition element for solid-to-beam and plate-to-beam connections. *Computers and Structures*, vol. 80, pp. 105–115.

Gmür, T. C.; Kauten, R. H. (1993): Three-dimensional solid to beam transition elements for structural dynamics analysis. *International Journal for Numerical Methods in Engineering*, vol. 36, pp. 1429–1444.

Gmür, T. C.; Schorderet, A. M. (1993): A set of three-dimensional solid to shell transition elements for structural dynamics. *Computers and Strucrures*, vol. 46, pp. 583–591.

Hodges, D. H. (2006): *Nonlinear composite beam theory*. American Institute of Aeronautics and Astronautics.

Hodges, D. H.; Ho, J. C.; Yu, W. (2008): The effect of taper on section constants for in-plane deformation of an isotropic strip. *Journal of Mechanics of Materials and Structures*, vol. 3, pp. 425 – 440.

Housner, J. M.; Aminpour, M. A.; DVavila, C.; Schiermeier, J. E.; Stroud, W. J.; Ransom, J. B.; Gillian, R. E. (1995): An interface element for global/local and substructuring analysis. In *Presented at the MSC 1995 World Users Conference, Los Angeles, CA*.

Kavous Jorabchi, J. D.; Suresh, K. (2009): Efficient and automated analysis of potentially slender structures. *Journal of Computing and Information Science in Engineering*, vol. 9.

Leon S. Johansen, E. L.; Kleist, J. (2009): Failure optimization of geometrically linear/nonlinear laminated composite structures using a two-step hierarchical model adaptivity. *Comput. Methods Appl. Mech. Engrg.*, vol. 198, pp. 2421–2438.

McCune, R. W.; Armstrong, C. G.; Robinson, D. J. (2000): Mixed-dimensional coupling in finite element models. *International Journal For Numerical Methods In Engineering*, vol. 49, pp. 725–750.

Monaghan, D. J.; Doherty, I. W.; Court, D. M.; Armstrong, C. G. (1998): Coupling 1d beams to 3d bodies. In *7th International Meshing Roundtable. Sandia National Laboratories, Dearborn, Michigan*.

N. Osawa, K. Hashimoto, J. S. T. N.; Suzuki, S. (2007): Study on shellsolid coupling fe analysis for fatigue assessment of ship structure. *Marine Structures*, vol. 20, pp. 143–163.

P. Mata, A. B.; Oller, S. (2008): Two-scale approach for the nonlinear dynamic analysis of rc structures with local non-prismatic parts. *Engineering Structures*, vol. 30, pp. 3667–3680.

Ransom, J. B.; McCleary, S. L.; Aminpour, M. A. (1993): A new interface element for connecting independently modelled substructures. In *AIAA/ASME/ASCE/AHS/ASC 34th Structures, Structural Dynamics, and Materials Conference, La Jolla, CA*.

Schiermeier, J. E.; Kansakar, R.; Mong, D.; Ransom, J. B.; Aminpour, M. A.; Stroud, W. J. (2002): p-version interface elements in global/local analysis. *International Journal For Numerical Methods In Engineering*, vol. 53, pp. 181–206.

Shephard, M. S. (1984): Linear multipoint constraints applied via transformation as part of a direct stiffness assembly process. *International Journal for Numerical Methods in Engineering*, vol. 20, pp. 2107–2112.

Shim, K. W.; Monaghan, D. J.; Armstrong, C. G. (2002): Mixed dimensional coupling in finite element stress analysis. *Engineering with Computers*, vol. 18, pp. 241–252.

Surana, K. S. (1979): Isoparametric elemetns for cross-sepctional properties and stress analysis of beams. *International Journal for Numerical Methods in Engineering*, vol. 14, pp. 475–497.

Surana, K. S. (1980): Transition finite-elements for axisymmetric stress-analysis. *International Journal for Numerical Methods in Engineering*, vol. 15, pp. 809–832.

Surana, K. S. (1980): Transition finite-elements for three dimensional stress analysis. *International Journal for Numerical Methods in Engineering*, vol. 15, pp. 991–1020.

Surana, K. S. (1982): Geometrically non-linear formulation for the three dimensional solid-shell transition finite elements. *Computers and Strucrures*, vol. 15, pp. 549–566.

Sylvain Bournival, Jean-Christophe CuilliÃ¨re, V. F. (2010): A mesh-geometry based method for coupling 1d and 3d elements. *Advances in Engineering Software*, vol. 41, pp. 838–858.

T.T. Robinson, C.; R.Fairey (2011): Automated mixed dimensional modelling from 2d and 3d cad models. *Finite Elements in Analysis and Design*, vol. 47, pp. 151–165.

Yu, W.; Hodges, D. H. (2004): Elasticity solutions versus asymptotic sectional analysis of homogeneous, isotropic, prismatic beams. *Journal of Applied Mechanics*, vol. 71, pp. 15–23.

Yu, W.; Hodges, D. H. (2005): Generalized timoshenko theory of the variational asymptotic beam sectional analysis. *Journal of the American Helicopter Society*, vol. 50, pp. 46–55.

Yu, W.; Hodges, D. H.; Volovoi, V. V.; Cesnik, C. E. S. (2002): On timoshenko-like modeling of initially curved and twisted composite beams. *International Journal of Solids and Structures*, vol. 39, pp. 5101–5121.

Yu, W.; Volovoi, V. V.; Hodges, D. H.; Hong, X. (2002): Validation of the variational asymptotic beam sectional analysis. *AIAA Journal*, vol. 40, pp. 2105–2113.